Synthesis and characterization of argyrodite solid electrolytes for all-solid-state Li-ion batteries

Zhang, Zhixia; Zhang, Long; Liu, Yanyan; Yu, Chuang; Yan, Xinlin; Xu, Bo; Wang, Li min

DOI
10.1016/j.jallcom.2018.03.027

Publication date
2018

Document Version
Accepted author manuscript

Published in
Journal of Alloys and Compounds

Accepted Manuscript

Synthesis and characterization of argyrodite solid electrolytes for all-solid-state Li-ion batteries

Zhixia Zhang, Long Zhang, Yanyan Liu, Chuang Yu, Xinlin Yan, Bo Xu, Li-min Wang

PII: S0925-8388(18)30886-7

DOI: 10.1016/j.jallcom.2018.03.027

Reference: JALCOM 45257

To appear in: *Journal of Alloys and Compounds*

Received Date: 19 December 2017

Revised Date: 1 March 2018

Accepted Date: 3 March 2018

Please cite this article as: Z. Zhang, L. Zhang, Y. Liu, C. Yu, X. Yan, B. Xu, L.-m. Wang, Synthesis and characterization of argyrodite solid electrolytes for all-solid-state Li-ion batteries, *Journal of Alloys and Compounds* (2018), doi: 10.1016/j.jallcom.2018.03.027.

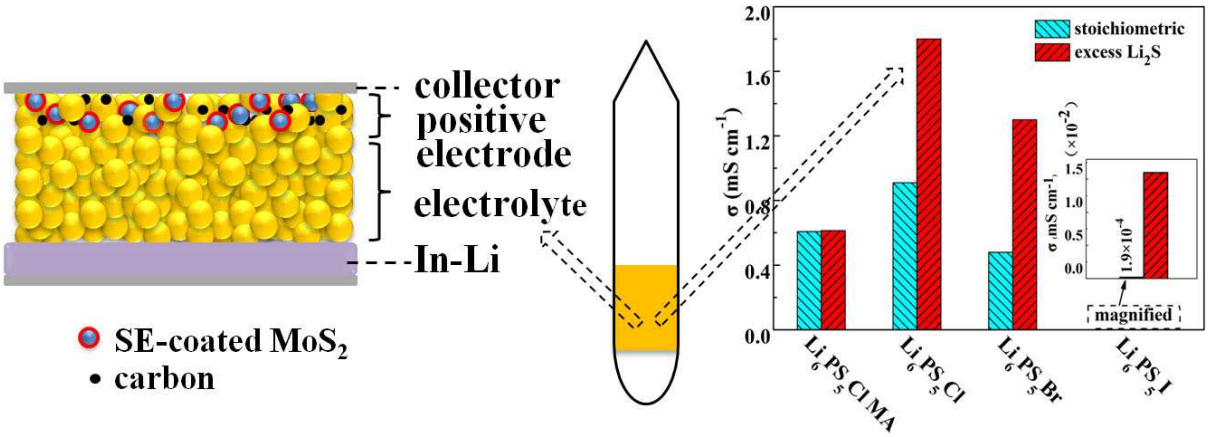

Synthesis and characterization of argyrodite solid electrolytes for all-solid-state Li-ion batteries

Zhixia Zhang[a], Long Zhang[a,*], Yanyan Liu[a], Chuang Yu[b], Xinlin Yan[c], Bo Xu[a], Li-min Wang[a]

[a]State Key Laboratory of Metastable Materials Science and Technology, Yanshan University, Qinhuangdao, Hebei 066004, China
[b]Department of Radiation Science and Technology, Delft University of Technology, Mekelweg 15, Delft 2629 JB, The Netherlands
[c]Institute of Solid State Physics, Vienna University of Technology, Wiedner Hauptstr. 8-10, 1040 Vienna, Austria

*Corresponding author. E-mail address: lzhang@ysu.edu.cn (Long Zhang)

ABSTRACT

Li_6PS_5X (X = Cl, Br, I) argyrodites possess high ionic conductivity but with rather scattered values due to various processing conditions. In this work, Li_6PS_5X solid electrolytes were prepared by solid-state sintering or mechanical alloying and optimized with or without excess Li_2S. Solid-state sintering prefers excess Li_2S, whereas mechanical alloying prefers stoichiometric Li_2S to synthesize high-purity samples with high ionic conductivity. Solid-state sintering is also more suitable than mechanical milling for high ionic conductivity. Li_6PS_5Cl with the highest ionic conductivity among Li_6PS_5X was comprehensively characterized for electrochemical performance and air stability. MoS_2/Li_6PS_5Cl all-solid-state batteries assembled with Li_6PS_5Cl-coated MoS_2 as cathode and with Li_6PS_5Cl as solid electrolyte demonstrate high capacity and good cycling stability.

Keywords: Argyrodites; Li_6PS_5Cl; All-solid-state batteries; Solid electrolytes; Sulfides

1. Introduction

Conventional lithium-ion batteries with liquid electrolytes limit their applications because of the safety concerns regarding flammability, leak, and toxicity of liquid electrolytes. Solid electrolytes (SEs) possess the advantages of good thermal stability, wide electrochemical windows, absence of leakage, and easy volumetric miniaturization [1-5]. Replacing liquid electrolytes by SEs to compose all-solid-state batteries is thus an effective way to solve the safety issues and a promising strategy for next-generation batteries with high energy density [6-9]. To achieve good electrochemical properties, an all-solid-state battery requires an SE possessing high ionic conductivity, low resistance at the electrolyte–electrode interface, and good structural and electrochemical stability [10, 11]. Among all promising candidates for all-solid-state lithium-ion batteries, sulfide-based SEs are especially attractive due to their high lithium-ion conductivity and good deformability, thereby making it easy to fabricate intimate contacts with active materials through a simple cold-pressing method without further high-temperature sintering process [12-15].

As a series of promising inorganic SEs, halogen-doped Li_6PS_5X (X = Cl, Br, I) argyrodites have attracted intensive attention due to their relatively high ionic conductivity and moderate electrochemical stability window [16-18]. However, the reported ionic conductivity values of Li_6PS_5X are still rather scattered in the range of 10^{-3} to 10^{-5} S cm^{-1} at room temperature even with the same X element, which is believed to be originated from various synthesis techniques and processing conditions [19]. The three common methods used to prepare Li_6PS_5X are (1) mechanical alloying

(ball milling) [20-25], (2) mechanical alloying followed by annealing to obtain high crystallinity [26-31], and (3) solid-state sintering [16, 32]. The first two methods are more popular because ball-milled powders have significantly smaller particle size than those prepared by hand-ground. Nevertheless, the sticky precursors contribute to the difficulty of the ball milling process because powders strongly adhere to the balls and jar's wall. On the other hand, solid-state sintering is a facile method feasible for mass production. This method is thus highly motivating to synthesize Li_6PS_5X through solid-state sintering with optimized processes.

A large contact area between electrode and SE powders is another consideration toward all-solid-state batteries with high electrochemical performance because a good electrode–electrolyte contact is favorable for low internal resistivity and can further increase energy density [15, 33]. However, obtaining a good contact through solid-state mixing is difficult because of the point contact between particles. Instead, SE coating on active materials is an effective way to realize a large contact area. Electrodes using SE-coated composites have been reported to achieve better electrochemical performance compared to non-coated active materials. For example, cathode materials of Li_6PS_5Cl-coated $LiCoO_2$ [24, 34], Li_6PS_5Br-coated $LiCo_{1/3}Ni_{1/3}Mn_{1/3}O_y$ [35], and Li_6PS_5Cl-coated Li_2S [36] using solution processes (EtOH as solvent) show higher capacities than those using a powder mixing method; Li_6PS_5Cl-coated $Li_4Ti_5O_{12}$ using 200#Paint as solvent also shows good electrode–electrolyte interface and improved electrochemical performance [28]. One of the key points when using solution processes is to develop solution-processable

SEs, which can be formed from a homogeneous solution using nontoxic and safe solvents of low boiling points , thus ensuring high ionic conductivity for the final product.

Transition metal sulfides with nanosheet microstructure are suitable for the solution-coating method because of the flat 2D morphology [37]. Additionally, sulfide active materials have good interfacial compatibility with sulfide electrolytes [38]. Especially, transition metal dichalcogenides provide many new opportunities in energy storage, including supercapacitors, lithium-/sodium-ion batteries, hydrogen storages, and electrochemical biosensors with advantages of large surface areas, metallic, semi-conducting electrical capabilities, and high sensitivity and selectivity [39, 40]. MoS_2, as a typical family member of transition metal dichalcogenide, possesses excellent properties in many fields [41, 42]. Previously, Chen *et al*. reported all-solid-state MoS_2/Li_6PS_5Br batteries with a high rate capability of up to 1 C and good capacity retention of 85% up to 700 cycles even though the microstructure of MoS_2 used in this literature has an irregular shape rather than nanosheet. Even the positive electrode composite was prepared by ball milling the mixture of MoS_2 and Li_6PS_5Br instead of a solution-based coating method [43].

The strategy of this work is to optimize Li_6PS_5X with various halogen elements and synthesis methods. The optimized material then used as coating-electrolyte coated on MoS_2 nanosheets. Herein, Li_6PS_5Cl, Li_6PS_5Br, and Li_6PS_5I were synthesized by a facile solid-state sintering method and optimized with and without excess Li_2S. Li_6PS_5Cl with excess Li_2S prepared through solid-state sintering is demonstrated to

have the highest ionic conductivity. Solid-state sintering is found to be superior to mechanical alloying in the current research. Li_6PS_5Cl shows good compatibility toward metallic Li. All-solid-state MoS_2/Li_6PS_5Cl/In-Li batteries assembled using SE-coated MoS_2 nanosheet show higher capacity and better cycling performance than those without SE coating.

2. Experiments

2.1. Synthesis of Li_6PS_5X

The Li_6PS_5X (X = Cl, Br, I) compounds were synthesized using a solid-state sintering method [44, 45]. Li_2S (Alfa Aesar, 99.9%), P_2S_5 (Aladdin, 99%), and LiX (X = Cl, Br, I; Alfa Aesar, 99.9%) powders were typically mixed according to the stoichiometric ratio followed by hand-grinding in an agate mortar. The mixture was loaded into a glassy carbon crucible, which was vacuum-sealed in a carbon-coated quartz tube. The mixture was then slowly heated to 600 °C at 0.3 °C/min to avoid extensive exothermal reaction and cooled down naturally in the furnace. The resultant ingot was ground in an agate mortar for further use. Additionally, Li_6PS_5X with 2 wt% excess Li_2S was prepared with the same procedure to evaluate the effect of Li loss due to volatilization at high temperatures [46].

Mechanically alloyed Li_6PS_5Cl was prepared through ball milling stoichiometric quantities of Li_2S (and Li_2S with 2 wt% excess), P_2S_5, and LiCl powders. The ball milling was carried out using a planetary ball mill (Fritsch, Pulverisette 7) with a stainless steel vial and balls. The rotation speed is 600 rpm, and the milling time is 24 h.

For easy comparison between various compositions and synthesis techniques, Li_6PS_5Cl, Li_6PS_5Br, and Li_6PS_5I with excess Li_2S prepared by solid-state sintering are designated as LPSC, LPSB, and LPSI, respectively; Li_6PS_5Cl prepared by mechanical alloying with and without excess Li_2S are designated as LPSC-MA and LPSC-MA-S, respectively; Li_6PS_5Cl with stoichiometric Li_2S prepared by solid-state sintering is designated as LPSC-S. Notably, LPSC shows the highest ionic conductivity and thus was used for further characterizations.

2.2. Materials characterization

X-ray diffraction (XRD) measurements were carried out with a Rigaku D/MAX-2500/PC (Cu Kα, 40 kV 200 mA). Rietveld refinements were performed using the FULLPROF program to determine the lattice parameters [47]. The specimens were loaded to holders in a glove box with Ar atmosphere and then sealed using Kapton films to prevent reaction with moisture and oxygen. Morphological characterizations were obtained with a scanning electron microscope (SEM, Hitachi S-4800 II FESEM) equipped with an energy dispersive spectrometry (EDS) instrument.

2.3. Electrochemical measurements

Electrochemical impedance spectroscopy (EIS) measurements were performed in a frequency range of 3 MHz−0.1 Hz at room temperature using a Princeton P4000 impedance analyzer. The pellets for the measurements were cold-pressed at approximately 300 MPa with indium foils placed on both sides of the pellets. The sandwiched pellets were then mounted on an air-tight two-electrode cell with two

stainless-steel rods as current collectors. A pellet with indium foils placed on both sides was exposed to the air (with a humidity of approximately 65%) for different time before the EIS measurements to test the air stability of the electrolyte.

The cyclic voltammetry (CV) measurements were carried out at voltages ranging from −0.5 V vs to 2.5 V vs at a scan rate of 0.05 mV s^{-1} in an asymmetric Pt/LPSC/Li cell, where Pt is a working electrode and Li is a counter/reference electrode. To evaluate the electrochemical stability of Li_6PS_5Cl toward lithium metal, lithium plating–stripping galvanostatic cycling tests were performed on a Li/LPSC/Li symmetric cell with a constant current density of 0.1 mA cm^{-2} on the LAND cell test instrument. The direct-current (DC) polarization tests were carried out to determine the lithium transference number with a constant voltage of 0.1 V using Princeton P4000. The nonblocking Li/LPSC/Li and the blocking Pt/LPSC/Pt cells used for DC polarization tests were assembled by placing Li or Pt foils on the two sides of cold -pressed LPSC pellet. A Faraday cage was used for the electrochemical measurements.

Li_6PS_5Cl-coated MoS_2 was prepared as follows. First, an as-synthesized Li_6PS_5Cl specimen was dissolved in anhydrous ethanol with intense stirring for 1 h at room temperature. A homogeneous dark brown EtOH solution was obtained. MoS_2 powders were then added to the solution to form a suspension with a mass ratio of MoS_2:Li_6PS_5Cl = 9:1. The mixture was finally heated under vacuum at 180 °C to form Li_6PS_5Cl-coated MoS_2, which was designated as LPSC-MoS_2. For assembly of MoS_2/Li_6PS_5Cl all-solid-state batteries, the composite positive electrode was prepared

by manually mixing Li_6PS_5Cl-coated MoS_2, LPSC, and AB powders in a weight ratio of 42:53:5. A bilayer pellet comprising the composite positive electrode (14 mg) and LPSC (120 mg) was obtained by cold-pressing under 300 MPa. In-Li foil was then attached to the bilayer pellet by pressing under 200 MPa. In-Li instead of Li negative electrode was used because the Li_6PS_5Cl electrolyte is finitely stable against metallic Li. Finally, two stainless steel rods were used on both sides of the pellet as current collectors.

The galvanostatic (dis)charge cycling of all-solid-state cells was performed in the voltage range of 0.1–3 V. The capacity was calculated based on the weight of active material (Li_6PS_5Cl-coated MoS_2). The EIS measurements of the cells were carried out on a Princeton P4000 electrochemical workstation from 1 MHz to 0.01 Hz by applying a potential of 10 mV.

3. Results and discussion

3.1. Optimization of Li_6PS_5X

XRD patterns of Li_6PS_5X where X = Cl, Br, I synthesized by solid-state sintering are illustrated in Fig. 1a. The halo patterns at low angles are obtained from the polyimide film used to isolate the samples from the air. All the samples are primarily of the argyrodite structure of F-43m symmetry, thereby indicating the successful synthesis of Li_6PS_5X via the solid-state sintering method. This method is feasible for mass production and avoids the strong adherence of precursors to the milling jar and balls during ball milling. The lattice parameters of Li_6PS_5X are 9.8890, 9.9973, and 10.0377 Å for the samples where X = Cl, Br, and I, respectively. The expansion of the

unit cell is expected due to an increased atomic radii from Cl, Br, and I. Fig. 1b shows the XRD patterns of Li_6PS_5Cl prepared by mechanical alloying or solid-state sintering with and without excess Li_2S. Mechanically alloyed samples (LPSC-MA and LPSC-MA-S) show broader peak-widths than the solid-state-sintered samples due to the small particle size after ball milling and improved crystallization of the sintered samples. Excess Li_2S demonstrates different effects on the structure of the final products. Regarding the samples prepared by solid-state sintering, excess Li_2S mitigates the impurity phase at 2θ = 29.0° on the profile for Li_6PS_5Cl with stoichiometric Li_2S (LPSC-S). On the contrary, excess Li_2S results in Li_2S impurity at 2θ = 26.9° in mechanically alloyed samples. This result indicates that some Li were lost during sintering even in a sealed quartz tube. These losses can be compensated by the Li addition, whereas the mechanically alloyed samples do not suffer from such issue.

The ionic conductivity values of Li_6PS_5X are compared in Fig. 1c. The excess Li_2S effectively improves the ionic conductivity of Li_6PS_5X prepared by solid-state sintering, especially for Li_6PS_5I, which has an improvement of two orders of magnitude. By contrast, the excess Li_2S shows a negligible effect on ionic conductivity for mechanically alloyed samples despite the Li_2S impurity phase induced by the excess Li_2S. Among Li_6PS_5X for either excess Li_2S or stoichiometric Li_2S, Li_6PS_5Cl demonstrates the highest ionic conductivity. However, the ionic conductivity decreases from 1.8 mS cm^{-1} for Li_6PS_5Cl with 2 wt% excess Li_2S to 0.8 mS cm^{-1} for Li_6PS_5Cl with 4 wt% excess Li_2S (not shown here). Therefore, 2 wt% is

the optimized value for Li_6PS_5Cl prepared by solid-state sintering. The room -temperature ionic conductivities of Li_6PS_5Cl, Li_6PS_5Br, and Li_6PS_5I with excess Li_2S are 1.8, 1.3, and 0.015 mS cm^{-1}, respectively, which are comparable to those of mechanically alloyed and annealed samples previously reported [17, 29]. The different ionic conductivities of Li_6PS_5X with different X can be attributed to the ordered/disordered structures induced by X elements [16, 32]. The ionic conductivity of all mechanically alloyed Li_6PS_5Cl samples is 0.61 mS cm^{-1}. The low values may be correlated to a large grain-boundary resistance and partial amorphization during ball milling [25]. The ionic conductivity of the mechanically alloyed samples may be improved by further annealing [30]. Given the high ionic conductivity of solid-state-sintered Li_6PS_5Cl with excess Li_2S, the morphology, air stability, and electrochemical characterization were performed using this sample (LPSC).

SEM images of the Li_6PS_5Cl morphology are displayed in Fig. 2. The morphologies of LPSC (Fig. 2a, b) and LPSC-BM-S (Fig. 2c, d) samples show a lamellar-like shape, but the sintered sample shows more agglomeration than the mechanically alloyed sample. The average particle size is 12 μm for the former and 8 μm for the latter sample, thus leading to higher ionic conductivity of the sintered sample than that of the mechanically alloyed sample. Moreover, the latter shows smaller grains than the former, which agrees with the XRD results.

3.2. Characterization of Li_6PS_5Cl

Fig. 3a shows the Arrhenius plot of the total ionic conductivity σ for LPSC in the temperature range from 25 °C to 80 °C. The total ionic conductivity is read from the

local minimal resistance at the intersection of the impedance spectra, which are displayed in the inset of Fig. 3a. The impedance spectra of the samples measured below 50 °C were fit with the equivalent circuit (R_SQ)Q. The resulting R_S is listed in Table 1. The fitting values are in accordance with the values directly read from the impedance spectra. Small semicircles were observed at high frequencies of impedance spectra and gradually disappeared with increasing temperature. This observation indicates that the overall resistance is dominated by bulk component at high temperatures. The steep linear spike at low frequencies indicates a behavior of typical ionic conductor. The linear dependence of logσ versus (1/T) follows the Arrhenius law, thereby confirming high purity and good thermal stability of LPSC over the measured temperature range. The ionic conductivity increases from 1.7 mS cm^{-1} at room temperature to 15 mS cm^{-1} at 80 °C. The activation energy E_a for Li^+ conduction was calculated from the slope of the linear Arrhenius plot using the following simplified equation [48]: $\sigma = A \exp(-E_a/k_B T)$, where A is the pre-exponential parameter, T is absolute temperature, and k_B is the Boltzmann constant. The calculated activation energy of LPSC is 0.35 eV, which is comparable to the previously reported results [17, 26]. The high ionic conductivity and low activation energy of LPSC are favorable for all-solid-state lithium-ion batteries with high electrochemical performance.

Air stability of Li_6PS_5Cl was tested because sulfides are generally sensitive to moisture. Fig. 3b shows XRD patterns of LPSC before and after exposure to air with a humidity of approximately 65% for 10 min. Several impurity peaks appeared after air

exposure due to the decomposition of Li_6PS_5Cl. Surprisingly, the decrease in ionic conductivity is not as bad as expected even after exposure to air for 24 h and shows a nonlinear dependence with exposure time, as depicted in Fig. 3c. The value decreases from 1.8 mS cm^{-1} for the pristine sample to 1.56, 1.43, and 0.87 mS cm^{-1} for air exposure for 10 min, 1 h, and 24 h, respectively. From this viewpoint, Li_6PS_5Cl can be sustained in air for a short time.

Apart from the ionic conductivity, the electrochemical window is also important for practical applications. Fig. 4a shows the CV curve of the Pt/LPSC/Li cell with a potential range of −0.5 V to 5 V versus Li/Li^+ at a scan rate of 5 mV s^{-1}. No reaction is observed up to 5 V other than lithium deposition and dissolution, which appeared nearby 0 V during cathodic and anodic scans. Thus, no severe decompositions of Li_6PS_5Cl over the measured voltage range are observed.

The symmetric cell of Li/LPSC/Li was assembled to evaluate the cyclability and long-time compatibility of Li_6PS_5Cl to metallic Li, as shown in Fig. 4b. The cell was cycled at room temperature with a current density of 0.1 mA cm^{-2}. The resulting voltage remained constant at approximately 17 mV over 4000 min (66 cycles), thereby indicating a stable interface and a small interfacial resistance between Li_6PS_5Cl and Li under the measured conditions. Although the theoretical study revealed that Li_6PS_5Cl is unstable toward Li [49], the Li_2S buffer layer formed from electrolyte decomposition during the first few cycles can protect the electrolyte from further decomposition due to the electrically insulating and ionically conductive feature of the buffer layers [50-53]. Although the same phenomenon cannot be

confirmed, the decomposed products of Li_2S, Li_3P, and Li_2O were detected in Ref. [54]. Unfortunately, detecting this decomposition of sulfide SE through CV and symmetric tests may be difficult [50].

Unlike liquid electrolytes, the anions are fixed in the frame of the structure in an inorganic SE; thus, only cations and electrons/holes contribute to the total conductivity. The DC polarization tests on symmetric cells at a constant voltage of 0.1 V were carried out to determine the lithium transference number, as shown in Fig. 4c. According to the nonblocking (Li/LPSC/Li) and the blocking (Pt/LPSC/Pt) test conditions, the overall conductivity and electronic conductivity of the LPSC were calculated to be 4.2×10^{-4} S cm^{-1} and 2.3×10^{-9} S cm^{-1}, respectively, which are comparable to those previously reported [55]. The electronic contribution is five orders of magnitude lower than the ionic contribution, thereby indicating that the lithium transference number of LPSC practically reaches unity. Thus, LPSC is a pure ion conductor. The conductivity measured by DC polarization is reasonably lower than that obtained by the AC impedance method due to different electrodes and contact conditions for the assembled cells [50].

3.3. Performance of MoS_2/LPSC/In all-solid-state batteries

Fig. 5 displays the SEM images and EDS mapping of the LPSC-coated MoS_2 powders (Figs 5a and c, respectively) compared with those of the pristine MoS_2 powders (Fig. 5b). The morphology of MoS_2 remains nearly unchanged before and after LPSC coating, which shows a spherical shape with a diameter of approximately 2.5 μm comprising nanosheets. Moreover, the uniform distributions of P, S, Cl, and

Mo elements are observed from the EDS mappings. These results verify the uniform deposition of Li_6PS_5Cl electrolyte on MoS_2 nanosheets.

Fig. 6 shows the first six cycles of CV curves for the MoS_2/LPSC/In cell at a scan rate of 0.05 mV s^{-1} in a potential range of –0.5–2.5 (Fig. 6a) and 0.1–3.1 (Fig. 6b) V versus In corresponding to the voltage of 0.1–3.1 (Fig. 6a) and 0.7–3.7 (Fig. 6a) V versus Li/Li^+, respectively, considering the potential difference of 0.6 V between In and Li. The two cells demonstrate similar electrochemical behaviors despite different voltage ranges. This finding indicates that the cell can be activated in the measured voltage range. The characteristic peaks of the CV curves for both potential ranges are in good agreement with the results based on previously reported liquid electrolytes [56]. The CV curves measured in the potential range of 0.1–3.1 V versus Li/Li^+ (Fig. 6a) are provided as an example. Two reduction peaks at around 1 V and 0.48 V and oxidation peaks at around 1.6 V and 2.25 V can be observed during the first cycle. In the cathodic sweep, the broad cathodic peak at approximately 1 V corresponds to the intercalation of Li^+ into MoS_2 interlayers, thus resulting in the formation of Li_xMoS_2; the peak at 0.48 V is attributed to the conversion from MoS_2 to Mo and Li_2S regarding the conversion reaction of $Li_xMoS_2 + (4-x)Li + (4-x)e^- \rightarrow Mo + 2Li_2S$, which is in accordance with MoS_2 data based on liquid electrolytes. In the following reverse scan, the weak peak at approximately 1.6 V is due to the incomplete oxidation of Mo metal and the other pronounced peaks at 2.25 V can be explained by the delithiation of Li_2S ($Li_2S - 2e^- \rightarrow 2Li^+ + S$). For the cathodic sweeps in the subsequent cycles, the peaks at 0.48 V and 1 V gradually disappeared along with the

appearance of new reduction peaks at approximately 1.7 V and 1.1 V induced by the formation of Li_2S through the new stepwise electrode reactions [43]. The nearly overlapped CV curves between 3rd and 4th scans indicate good reversibility of the MoS_2/LPSC/In-Li cell.

The galvanostatic charge–discharge profiles of the MoS_2/LPSC/In-Li cell with SE-coated MoS_2 as positive electrode are shown in Fig. 7a. Based on the CV results, the cell was tested in the voltage range of 0.1–3 V versus In-Li at a current density of 0.13 mA cm^{-2} based on the area of the In-Li at room temperature. An initial discharge capacity of 520 mAh g^{-1} is achieved, and 79% of the inserted Li can be reversibly delithiated with a charge capacity of 410 mAh g^{-1}. The capacity decay can be attributed to the volume expansion inside the battery due to the redox reaction of $MoS_2 + 4Li \rightarrow Mo + 2Li_2S$ [43] and the formation of SEI film and Li incorporation into SEI, which were observed in MoS_2 cells based on liquid electrolytes [57, 58]. The second lithiation delivers a capacity of 374 mAh g^{-1} and 90.7% is reversible in the second charging process. The charge–discharge profiles are nearly overlapped from the third cycle, thereby indicating a stable lithiation and delithiation process.

The rate capability and cycling stability tests (Fig. 7b) were performed on MoS_2/LPSC/In-Li cells between 0.1 V and 3 V at room temperature. Fig. 7c magnifies the curves for the rate capability tests. The cell delivers a stable capacity of 350 mAh g^{-1} at the current density of 0.13 mA cm^{-2} and a slight decrease when the current density is doubled. The capacity is still maintained at 241 mAh g^{-1} when the current density increases to 1.04 mA cm^{-2} and recovers back to 346 mAh g^{-1} when the

current density turns back to 0.13 mA cm^{-2}. Moreover, the cell demonstrates a superior cycling stability with a capacity of 200 mAh g^{-1} at a current density as high as 1.04 mA cm^{-2}.

EIS measurements were employed to understand the superior rate capability of the MoS_2/LPSC/In-Li cell. Fig. 8 shows the Nyquist plots of the cell before and after cycling tests (259 cycles). The solid symbols represent the experiment data, and the lines represent the fits based on the equivalent circuit R(RQ)W. The curves comprise the following three parts: (1) the intercepts of the curves on the *x*-axis at high frequencies related to the bulk resistance R_S; (2) the depressed semicircles at middle frequencies associated with charge-transfer resistance R_{ct}; and (3) the straight lines at low frequencies associated with the Warburg impedance corresponding to the mass transfer resistance [59]. R_S (Table 1) decreases from 41 Ω to 28 Ω after 259 cycles, which is beneficial for the reduced resistance due to an activated sulfide cathode and the presence of Mo metal after cycling [57, 60].

4. Conclusions

The argyrodite Li_6PS_5X (X = Cl, Br, I) SEs were synthesized by solid-state sintering or mechanical milling and optimized with and without excess Li_2S. Different SEM morphologies were observed in samples prepared with different synthesis methods. The excess Li_2S in raw materials is beneficial to obtain high-purity samples with high ionic conductivity by the solid-state sintering method, but it leads to Li_2S impurity in samples synthesized by mechanical milling even if the Li_2S impurity does not affect their ionic conductivity. The loss of Li_2S should be compensated during the

high-temperature heat treatment, especially for Li_6PS_5I. Li_6PS_5Cl shows the highest ionic conductivity among Li_6PS_5X. Li_6PS_5Cl synthesized by solid-state sintering shows a higher ionic conductivity than those by mechanical milling. Although Li_6PS_5Cl is hydrolyzed in air, the ionic conductivity is not severely degraded after air exposure for 24 h. The electrochemical characterizations revealed that Li_6PS_5Cl is a pure ionic conductor with a large electrochemical window and relatively good stability toward metallic Li. All-solid-state cells assembled using Li_6PS_5Cl-coated MoS_2 as cathode and Li_6PS_5Cl as electrolyte have high capacity and good cycling stability.

Acknowledgments

This work was supported by the National Science Foundation of China (51525205), the Foundation of Higher Education of Hebei (ZD2016033), and Natural Science Foundation of Hebei Province (E2018203301).

References

[1] A. Manthiram, X. Yu, S. Wang, Lithium battery chemistries enabled by solid-state electrolytes, Nat. Rev. Mater. 2 (2017) 16103.

[2] X. Judez, H. Zhang, C. Li, G.G. Eshetu, J.A.G. Marcos, M. Armand, L.M.R. Martinez, Review—Solid electrolytes for safe and high energy density lithium-sulfur batteries: promises and challenges, J. Electrochem. Soc. 165 (2018) A6008–A6016.

[3] Z. Ma, H.G. Xue, S.P. Guo, Recent achievements on sulfide-type solid electrolytes: crystal structures and electrochemical performance, J. Mater. Sci. 53 (2018) 3927–3938.

[4] A. Hayashi, A. Sakuda, M. Tatsumisago, Development of sulfide solid electrolytes and interface formation processes for bulk-type all-solid-state Li and Na batteries, Front. Energy Res. 4 (2016) 25.

[5] B.V. Lotsch, J. Maier, Relevance of solid electrolytes for lithium-based batteries: a realistic view, J. Electroceram. 38 (2017) 128–141.

[6] Q. Zhang, K. Liu, F. Ding, X. Liu, Recent advances in solid polymer electrolytes for lithium batteries, Nano Res. 10 (2017) 4139–4174.

[7] C. Sun, J. Liu, Y. Gong, D.P. Wilkinson, J. Zhang, Recent advances in all-solid-state rechargeable

lithium batteries, Nano Energy 33 (2017) 363–386.

[8] H. Hou, Q. Xu, Y. Pang, L. Li, J. Wang, C. Zhang, C. Sun, Efficient storing energy harvested by triboelectric nanogenerators using a safe and durable all-solid-state sodium-ion battery, Adv. Sci. 4 (2017) 1700072.

[9] Y. Zhang, J. Lai, Y. Gong, Y. Hu, J. Liu, C. Sun, Z.L. Wang, A safe high-performance all-solid-state lithium-vanadium battery with a freestanding V_2O_5 nanowire composite paper cathode, ACS Appl. Mater. Interfaces 8 (2016) 34309–34316.

[10] Y.Z. Sun, J.Q. Huang, C.Z. Zhao, Q. Zhang, A review of solid electrolytes for safe lithium-sulfur batteries, Sci. China Chem. 60 (2017) 1508–1526.

[11] J.F. Wu, W.K. Pang, V.K. Peterson, L. Wei, X. Guo, Garnet-Type fast Li-ion conductors with high ionic conductivities for all-solid-state batteries, ACS Appl. Mater. Interfaces 9 (2017) 12416–12468.

[12] X. Sun, Y. Sun, F. Cao, X. Li, S. Sun, T. Liu, J. Wu, Preparation, characterization and ionic conductivity studies of composite sulfide solid electrolyte, J. Alloys Compd. 727 (2017) 1136–1141.

[13] K.H. Park, D.Y. Oh, Y.E. Choi, Y.J. Nam, L. Han, J.Y. Kim, H. Xin, F. Lin, S.M. Oh, Y.S. Jung, Solution-processable glass LiI-Li_4SnS_4 superionic conductors for all-solid-state Li-ion batteries, Adv. Mater. 28 (2016) 1874–1883.

[14] X. Wu, M.E. Kazzi, C. Villevieille, Surface and morphological investigation of the electrode/electrolyte properties in an all-solid-state battery using a Li_2S-P_2S_5 solid electrolyte, J. Electroceram. 38 (2017) 207–214.

[15] R.C. Xu, X.L. Wang, S.Z. Zhang, Y. Xia, X.H. Xia, J.B. Wu, J.P. Tu, Rational coating of $Li_7P_3S_{11}$ solid electrolyte on MoS_2 electrode for all-solidstate lithium ion batteries, J. Power Sources 374 (2018) 107–112.

[16] H.J. Deiseroth, S.T. Kong, H. Eckert, J. Vannahme, C. Reiner, T. Zaiss, M. Schlosser, Li_6PS_5X: a class of crystalline Li-rich solids with an unusually high Li^+ mobility, Angew. Chem. 47 (2008) 755–758.

[17] S. Boulineau, M. Courty, J.-M. Tarascon, V. Viallet, Mechanochemical synthesis of Li-argyrodite Li_6PS_5X (X = Cl, Br, I) as sulfur-based solid electrolytes for all solid state batteries application, Solid State Ionics 221 (2012) 1–5.

[18] H.J. Deiseroth, J. Maier, K. Weichert, V. Nickel, S.T. Kong, C. Reiner, Li_7PS_6 and Li_6PS_5X (X: Cl, Br, I): Possible three-dimensional diffusion pathways for lithium ions and temperature dependence of the ionic conductivity by impedance measurements, Z. ANORG. ALLG. CHEM. 637 (2011) 1287–1294.

[19] Z.Wang, G.S, Theoretical design of solid electrolytes with superb ionic conductivity alloying effect on Li^+ transportation in cubic Li_6PA_5X chalcogenides, J. Mater. Chem. A 5 (2017) 21846–21875.

[20] J. Auvergniot, A. Cassel, J.-B. Ledeuil, V. Viallet, V. Seznec, R. Dedryvère, Interface stability of argyrodite Li_6PS_5Cl toward $LiCoO_2$, $LiNi_{1/3}Co_{1/3}Mn_{1/3}O_2$, and $LiMn_2O_4$ in bulk all-solid-state batteries, Chem. Mater. 29 (2017) 3883–3890.

[21] J. Auvergniot, A. Cassel, D. Foix, V. Viallet, V. Seznec, R. Dedryvère, Redox activity of argyrodite Li_6PS_5Cl electrolyte in all-solid-state Li-ion battery: An XPS study, Solid State Ionics 300 (2017) 78–85.

[22] S. Boulineau, J.M. Tarascon, J.B. Leriche, V. Viallet, Electrochemical properties of all-solid-state lithium secondary batteries using Li-argyrodite Li_6PS_5Cl as solid electrolyte, Solid State Ionics 242 (2013) 45–48.

[23] R.P. Rao, N. Sharma, V.K. Peterson, S. Adams, Formation and conductivity studies of lithium argyrodite solid electrolytes using in-situ neutron diffraction, Solid State Ionics 230 (2013) 72–76.

[24] S. Yubuchi, S. Teragawa, K. Aso, K. Tadanaga, A. Hayashi, M. Tatsumisago, Preparation of high lithium-ion conducting Li_6PS_5Cl solid electrolyte from ethanol solution for all-solid-state lithium

batteries, J. Power Sources 293 (2015) 941–945.
[25] C. Yu, S. Ganapathy, E.R.H. van Eck, L. van Eijck, S. Basak, Y. Liu, L. Zhang, H.W. Zandbergen, M. Wagemaker, Revealing the relation between the structure, Li-ion conductivity and solid-state battery performance of the argyrodite Li_6PS_5Br solid electrolyte, J. Mater. Chem. A 5 (2017) 21178–21188.
[26] C. Yu, S. Ganapathy, N.J. de Klerk, I. Roslon, E.R. van Eck, A.P. Kentgens, M. Wagemaker, Unravelling Li-Ion transport from picoseconds to seconds: Bulk versus interfaces in an argyrodite Li_6PS_5Cl-Li_2S all-solid-state Li-ion battery, J. Am. Chem. Soc. 138 (2016) 11192–11201.
[27] C. Yu, L. van Eijck, S. Ganapathy, M. Wagemaker, Synthesis, structure and electrochemical performance of the argyrodite Li_6PS_5Cl solid electrolyte for Li-ion solid state batteries, Electrochim. Acta 215 (2016) 93–99.
[28] A. Hwang, Y. Ma, Y. Cao, L. Wang, X.Q. Cheng, P.J. Zuo, C.Y. Du, Y.Z. Gao, G.P. Yin, Fabrication and electrochemical properties of $Li_4Ti_5O_{12}$@Li_6PS_5Cl for all-solid-state lithium batteries using simple mechanical method, Int. J. Electrochem. Sci. 12 (2017) 7795–7806.
[29] R.P. Rao, S. Adams, Studies of lithium argyrodite solid electrolytes for all-solid-state batteries, Phys. Status Solidi A 208 (2011) 1804–1807.
[30] P.R. Rayavarapu, N. Sharma, V.K. Peterson, S. Adams, Variation in structure and Li^+-ion migration in argyrodite-type Li_6PS_5X (X = Cl, Br, I) solid electrolytes, J. Solid State Electrochem. 16 (2011) 1807–1813.
[31] M. Chen, R.P. Rao, S. Adams, High capacity all-solid-state Cu–Li_2S/Li_6PS_5Br/In batteries, Solid State Ionics 262 (2014) 183–187.
[32] M.A. Kraft, S.P. Culver, M. Calderon, F. Bocher, T. Krauskopf, A. Senyshyn, C. Dietrich, A. Zevalkink, J. Janek, W.G. Zeier, Influence of lattice polarizability on the ionic conductivity in the lithium superionic argyrodites Li_6PS_5X (X = Cl, Br, I), J. Am. Chem. Soc. 139 (2017) 10909–10918.
[33] Y. Ito, S. Yamakawa, A. Hayashi, M. Tatsumisago, Effects of the microstructure of solid-electrolytecoated $LiCoO_2$ on its discharge properties in allsolid-state lithium batteries, J. Mater. Chem. A 5 (2017) 10658–10668.
[34] D.H. Kim, D.Y. Oh, K.H. Park, Y.E. Choi, Y.J. Nam, H.A. Lee, S.M. Lee, Y.S. Jung, Infiltration of solution-processable solid electrolytes into conventional Li-ion-battery electrodes for all-solid-state Li-ion batteries, Nano Lett. 17 (2017) 3013–3020.
[35] S. Chida, A. Miura, N.C. Rosero-Navarro, M. Higuchi, N.H.H. Phuc, H. Muto, A. Matsuda, K. Tadanaga, Liquid-phase synthesis of Li_6PS_5Br using ultrasonication and application to cathode composite electrodes in all-solid-state batteries, Ceram. Int. 44 (2018) 742–746.
[36] F. Han, J. Yue, X. Fan, T. Gao, C. Luo, Z. Ma, L. Suo, C. Wang, High-Performance all-solid-state lithium-sulfur battery enabled by a mixed-conductive Li_2S nanocomposite, Nano Lett. 16 (2016) 4521–4527.
[37] X. Yao, D. Liu, C. Wang, P. Long, G. Peng, Y.S. Hu, H. Li, L. Chen, X. Xu, High-energy all-solid-state lithium batteries with ultralong cycle life, Nano Lett. 16 (2016) 7148–7154.
[38] K. Aso, A. Sakuda, A. Hayashi, M. Tatsumisago, All-solid-state lithium secondary batteries using NiS-carbon fiber composite electrodes coated with Li_2S-P_2S_5 solid electrolytes by pulsed laser deposition, ACS Appl. Mater. Interfaces 5 (2013) 686–690.
[39] Y.-P. Gao, X. Wu, K.-J. Huang, L.-L. Xing, Y.-Y. Zhang, L. Liu, Two-dimensional transition metal diseleniums for energy storage application: a review of recent developments, CrystEngComm 19 (2017) 404–418.
[40] Y.H. Wang, K.J. Huang, X. Wu, Recent advances in transition-metal dichalcogenides based

electrochemical biosensors: A review, Biosens. Bioelectron. 97 (2017) 305–316.
[41] W.J. Zhang, K.J. Huang, A review of recent progress in molybdenum disulfide-based supercapacitors and batteries, Inorg. Chem. Front. 4 (2017) 1602.
[42] K.J. Huang, L. Wang, J.Z. Zhang, L.L. Wang, Y.P. Mo, One-step preparation of layered molybdenum disulfide/multi-walled carbon nanotube composites for enhanced performance supercapacitor, Energy 67 (2014) 234–240.
[43] M.H. Chen, X.S.Yin, M.V. Reddy, S. Adams, All-solid-state MoS_2 Li_6PS_5Br In-Li batteries as a novel type of Li/S battery, J. Mater. Chem. A 3 (2015) 10698–10702.
[44] L. Zhang, K. Yang, J. Mi, L. Lu, L. Zhao, L. Wang, Y. Li, H. Zeng, Na_3PSe_4: A novel chalcogenide solid electrolyte with high ionic conductivity, Adv. Energy Mater. 5 (2015) 1501294.
[45] L. Zhang, D. Zhang, K. Yang, X. Yan, L. Wang, J. Mi, B. Xu, Y. Li, Vacancy-contained tetragonal Na_3SbS_4 superionic conductor, Adv. Sci. 3 (2016) 1600089.
[46] T. Matsumura, K. Nakano, R. Kanno, A. Hirano, N. Imanishi, Y. Takeda, Nickel sulfides as a cathode for all-solid-state ceramic lithium batteries, J. Power Sources 174 (2007) 632–636.
[47] X. Li, B. Xu, L. Zhang, F. Duan, X. Yan, J. Yang, Y. Tian, Synthesis of iodine filled $CoSb_3$ with extremely low thermal conductivity, J. Alloys Compds. 615 (2014) 177–180.
[48] K. Yang, J.Y. Dong, L. Zhang, Y.M. Li, L.M. Wang, Dual Doping: An effective method to enhance the electrochemical properties of $Li_{10}GeP_2S_{12}$-based solid electrolytes, J. Am. Ceram. Soc. 98 (2015) 3831–3835.
[49] T. Cheng, B.V. Merinov, S. Morozov, W.A. Goddard, Quantum mechanics reactive dynamics study of solid Li-electrode/Li_6PS_5Cl-electrolyte interface, ACS Energy Lett. 2 (2017) 1454–1459.
[50] Y. Tao, S. Chen, D. Liu, G. Peng, X. Yao, X. Xu, Lithium superionic conducting oxysulfide solid electrolyte with excellent stability against Lithium metal for all-solid-state cells, J. Electrochem. Soc. 163 (2015) A96–A101.
[51] N.D. Lepley, N.A.W. Holzwarth, Y.A. Du, Structures, Li^+mobilities, and interfacial properties of solid electrolytes Li_3PS_4 and Li_3PO_4 from first principles, Phys. Rev. B 88 (2013) 104103.
[52] Z. Deng, Z. Zhu, I.-H. Chu, S.P. Ong, Data-driven first-principles methods for the study and design of alkali superionic conductors, Chem. Mater. 29 (2016) 281–288.
[53] Z. Wang, G.S. Shao, Theoretical design of solid electrolytes with superb ionic conductivity alloying effect on Li^+ transportation in cubic Li_6PA_5X chalcogenides, J. Mater. Chem. A 5 (2017) 21846–21857.
[54] S. Wenzel, S.J. Sedlmaier, C. Dietrich, W.G. Zeier, J. Janek, Interfacial reactivity and interphase growth of argyrodite solid electrolytes at lithium metal electrodes, Solid State Ionics (2017).
[55] F. Stadler, C. Fietek, Crystalline halide substituted Li-argyrodites as solid electrolytes for lithium secondary batteries, Electrochem. Soc. 25 (2010) 177–183.
[56] K. Chang, D. Geng, X. Li, J. Yang, Y. Tang, M. Cai, R. Li, X. Sun, Ultrathin MoS_2/Nitrogen-doped graphene nanosheets with highly reversible lithium storage, Adv. Energy Mater. 3 (2013) 839–844.
[57] J. Xiao, X. Wang, X.-Q. Yang, S. Xun, G. Liu, P.K. Koech, J. Liu, J.P. Lemmon, Electrochemically induced high capacity displacement reaction of PEO/MoS_2/Graphene nanocomposites with lithium, Adv. Funct. Mater. 21 (2011) 2840–2846.
[58] Y. Liu, L. Zhang, H. Wang, C. Yu, X. Yan, Q. Liu, B. Xu, L.-m. Wang, Synthesis of severe lattice distorted MoS_2 coupled with hetero-bonds as anode for superior lithium-ion batteries, Electrochim. Acta, 262 (2018) 162–172.
[59] X. Li, X. Cheng, M. Gao, D. Ren, Y. Liu, Z. Guo, C. Shang, L. Sun, H. Pan, Amylose-Derived macrohollow core and microporous shell carbon spheres as sulfur host for superior lithium-sulfur

battery cathodes, ACS Appl. Mater. Interfaces 9 (2017) 10717–10729.
[60] K. Cai, M.-K. Song, E.J. Cairns, Y. Zhang, Nanostructured Li_2S–C composites as cathode material for high-energy lithium/sulfur batteries, Nano Lett. 12 (2012) 6474–6479.

Figure Captions

Fig. 1. (a) XRD patterns of Li_6PS_5Cl (LPSC), Li_6PS_5Br (LPSB), and Li_6PS_5I (LPSI) with excess Li_2S prepared by solid-state sintering. (b) XRD patterns of Li_6PS_5Cl prepared by mechanical alloying or solid-state sintering with and without excess Li_2S. (c) Ionic conductivities of Li_6PS_5X (X = Cl, Br, I) with and without excess Li_2S. The inset scales out the *y*-axis of Li_6PS_5I.

Fig. 2. (a,b) SEM images of solid-state sintered Li_6PS_5Cl with excess Li_2S. (c,d) SEM images of mechanically alloyed Li_6PS_5Cl.

Fig. 3. (a) Arrhenius conductivity plot of LPSC from 25 to 80 °C. The inset displays the impedance spectra of LPSC measured at different temperatures. The spectra measured at 25 and 40 °C were fitted with the circuit ($(R_SQ)Q$). (b) XRD patterns of LPSC before and after exposing to air for 10 min (LPSC-AIR). (c) Ionic conductivity of air-exposed LPSC as a function of exposure time. The inset shows the Nyquist impedance plots and fit results ($(R_SQ)Q$) of LPSC exposed to air for different time.

Fig. 4. (a) Cyclic voltammogram of Pt/LPSC/Li cell at a scanning rate of 2 mV/s between −0.5 and 5 V. (b) Galvanostatic cycling of Li/LPSC/Li symmetric cell with a current density of 0.1 mA cm^{-2} (c) DC polarization current as a function of time with a constant voltage of 0.1 V under blocking (Pt/LPSC/Pt, lower panel) and nonblocking (Li/LPSC/Li, upper panel) conditions at room temperature.

Fig. 5. SEM image of LPSC-coated MoS_2 (a) and compared with that of pristine MoS_2 (b). (c) EDS mapping of LPSC-coated MoS_2.

Fig. 6. Cyclic voltammograms of the all-solid-state SE-coate MoS_2/LPSC/In-Li cell at a scanning rate of 0.05 mV s^{-1} in a voltage range of -0.5–2.5V vs. In-Li (a) and 0–3V vs. In-Li (b).

Fig. 7. (a) Galvanostatic charge-discharge profiles of selected cycles for the cells with SE-coated MoS_2 electrodes tested at current densities of 0.13 mA cm^{-2}. (b) Cycling performance and Coulombic efficiency for the cells with SE-coated MoS_2 electrode tested at various current densities .(c) Magnification of the cycling performance and the Coulombic efficiency from 1 to 25 cycles.

Fig. 8. Impedance spectra and fits of the all-solid-state batteries with SE-coated MoS_2 tested before and after 259 cycles at the room temperature.

Table 1 The total resistances obtained from fit results (R_S) and directed read (R_{read}) from the local minimal resistance at the intersection of the impedance spectrum.

	Measured Temperature In the inset of Fig. 3a			Air exposure time In the inset of Fig. 3c			Cycling In Fig. 8	
	25 °C	40 °C	50 °C	10 min	1 h	24 h	Before	After
$R_S(\Omega)$	140±1	69±1	42±1	187±1	192±1	397±1	41±1	28±1
$R_{read}(\Omega)$	134	68	42	182	194	399	–	–

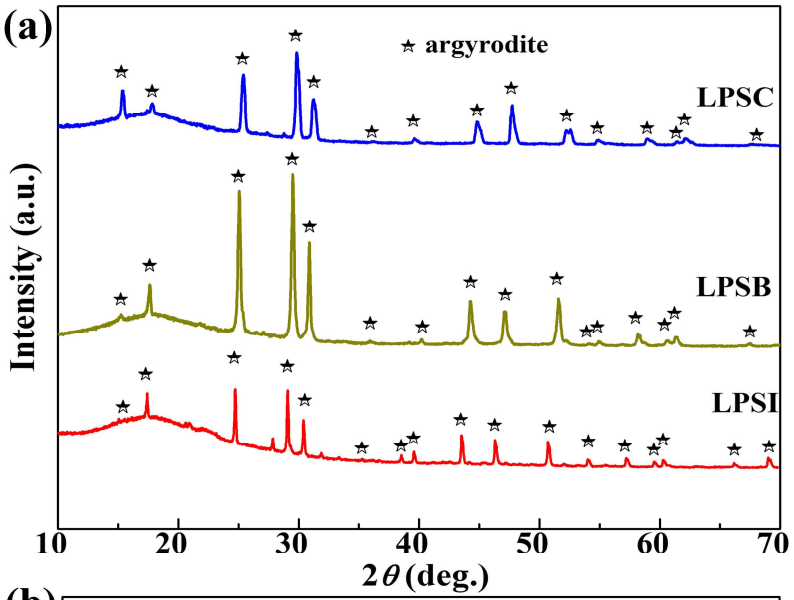
(a)
argyrodite
LPSC
LPSB
LPSI
Intensity (a.u.)
10
20
30
40
50
60
70
2θ (deg.)

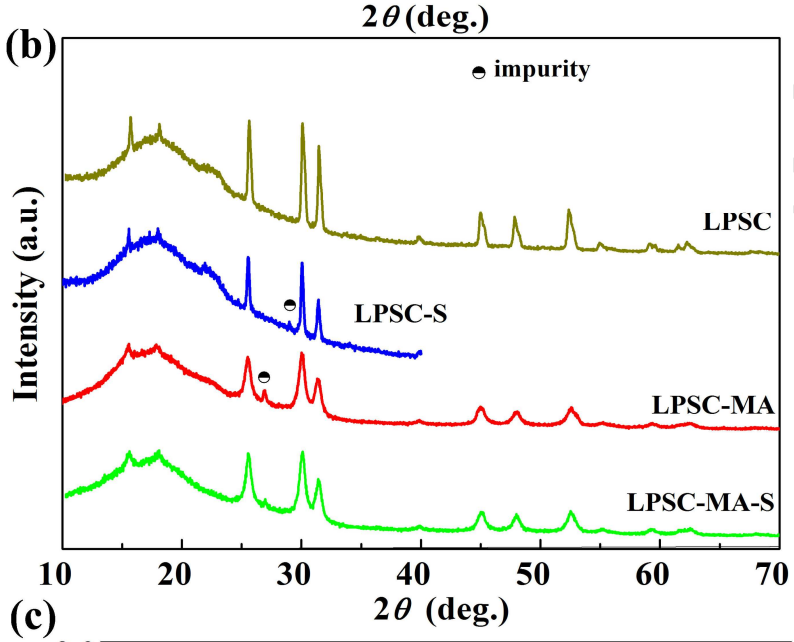
(b)
impurity
LPSC
LPSC-S
LPSC-MA
LPSC-MA-S
Intensity (a.u.)
10
20
30
40
50
60
70
2θ (deg.)

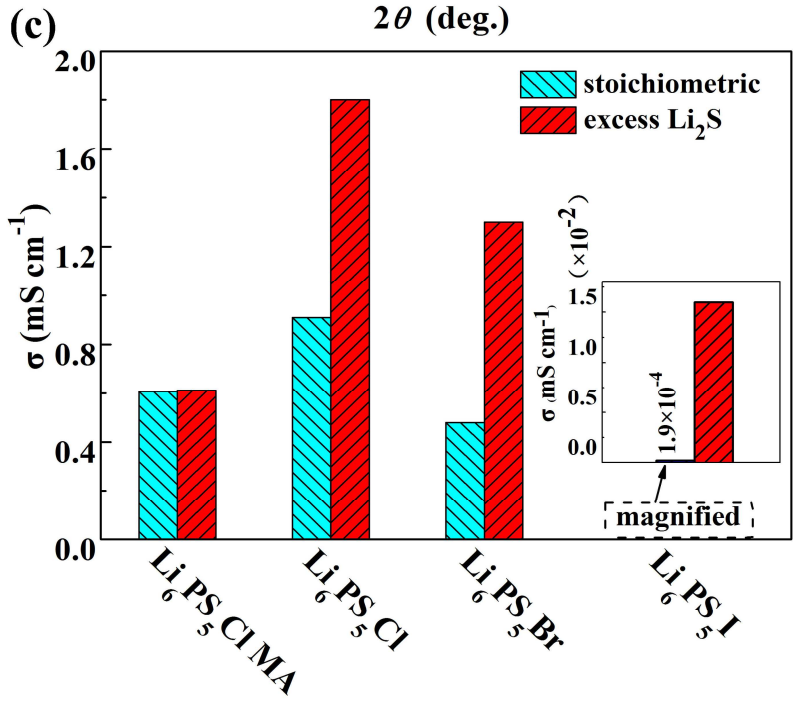
(c)
stoichiometric
excess Li2S
σ (mS cm-1)
2.0
1.6
1.2
0.8
0.4
0.0
σ (mS cm-1) (×10-2)
1.5
1.0
0.5
0.0
1.9×10-4
magnified
Li6PS5Cl MA
Li6PS5Cl
Li6PS5Br
Li6PS5I

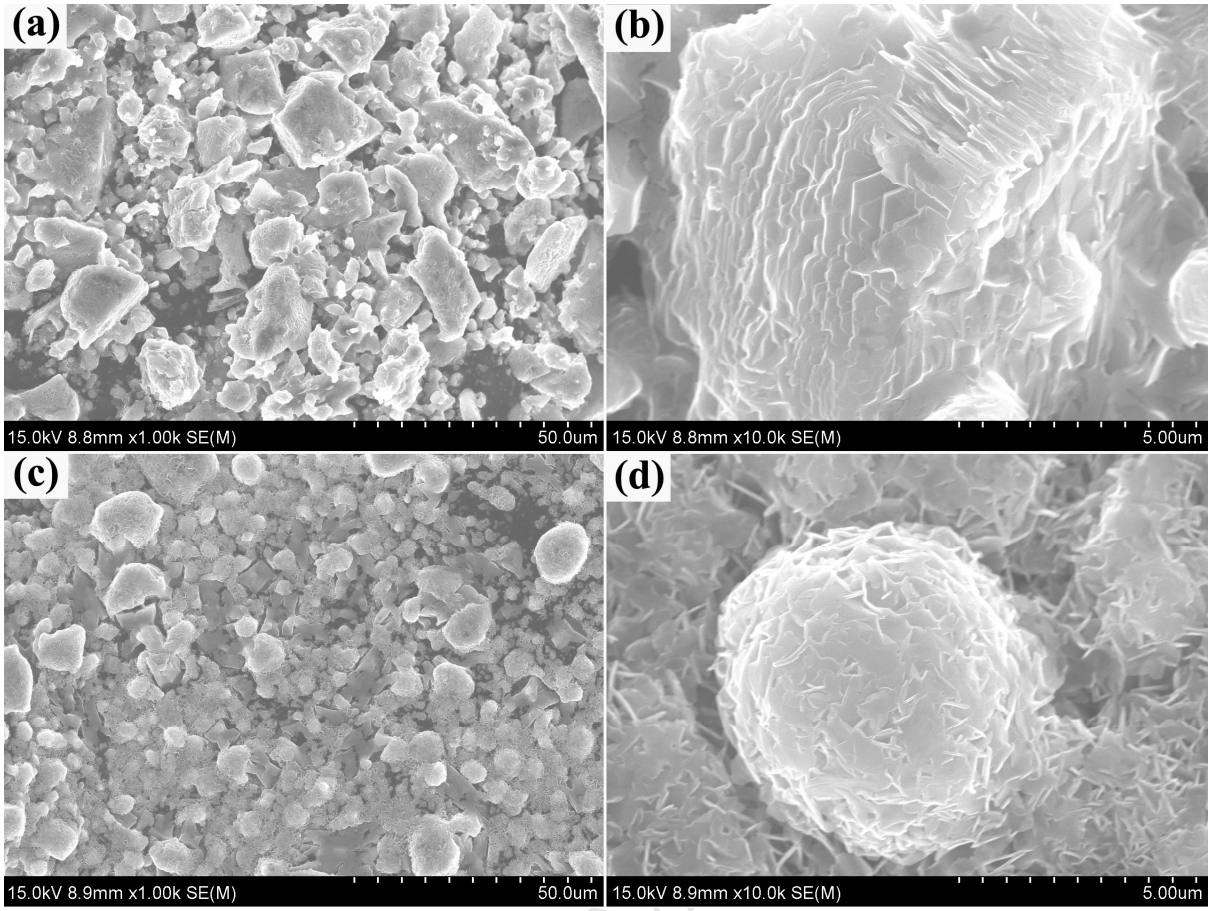

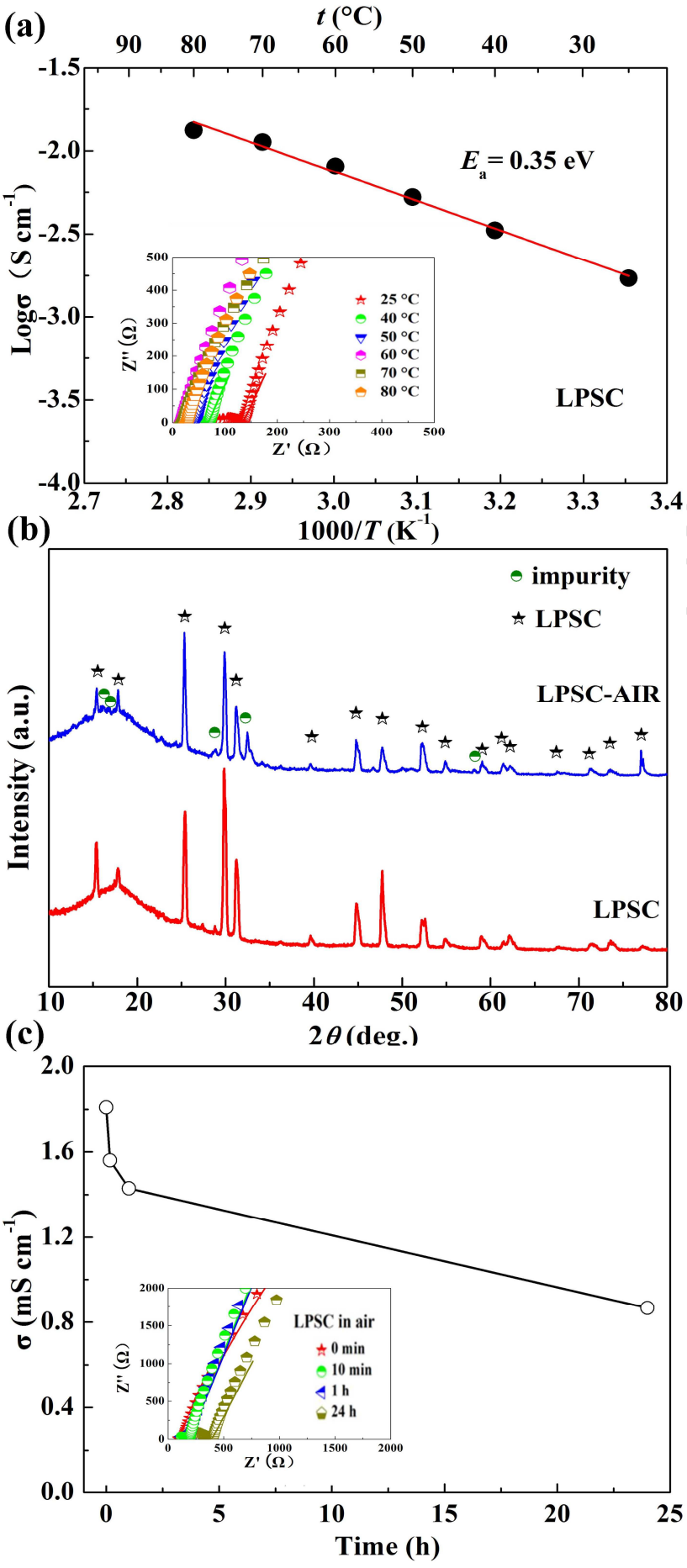
(a)
t (°C)
90 80 70 60 50 40 30
-1.5
-2.0
-2.5
-3.0
-3.5
-4.0
Logσ (S cm-1)
Ea = 0.35 eV
LPSC
25 °C
40 °C
50 °C
60 °C
70 °C
80 °C
Z'' (Ω)
Z' (Ω)
2.7 2.8 2.9 3.0 3.1 3.2 3.3 3.4
1000/T (K-1)
(b)
impurity
LPSC
LPSC-AIR
LPSC
Intensity (a.u.)
10 20 30 40 50 60 70 80
2θ (deg.)
(c)
2.0
1.6
1.2
0.8
0.4
0.0
σ (mS cm-1)
LPSC in air
0 min
10 min
1 h
24 h
Z'' (Ω)
Z' (Ω)
0 5 10 15 20 25
Time (h)

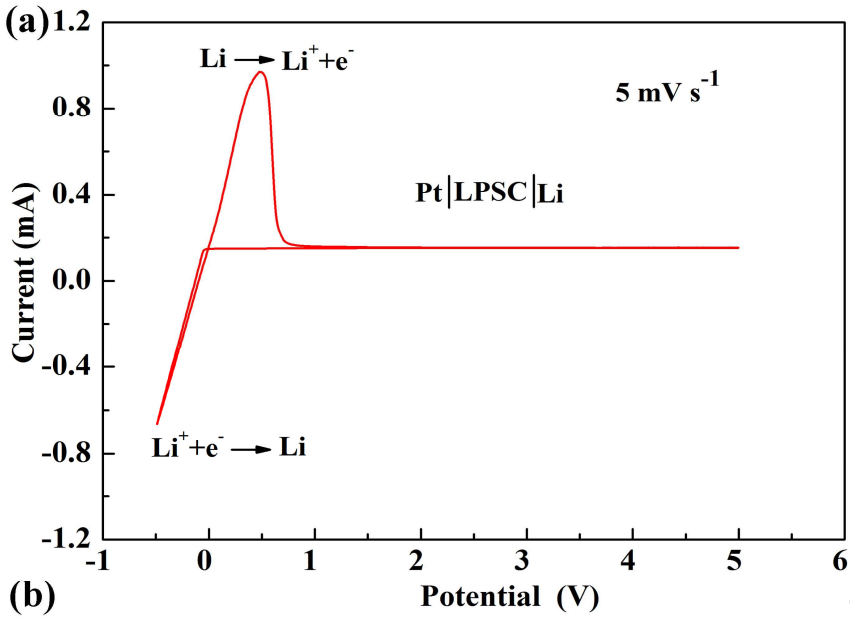
(a)
Li → Li+ +e-
5 mV s-1
Pt|LPSC|Li
Li+ +e- → Li
Current (mA)
Potential (V)

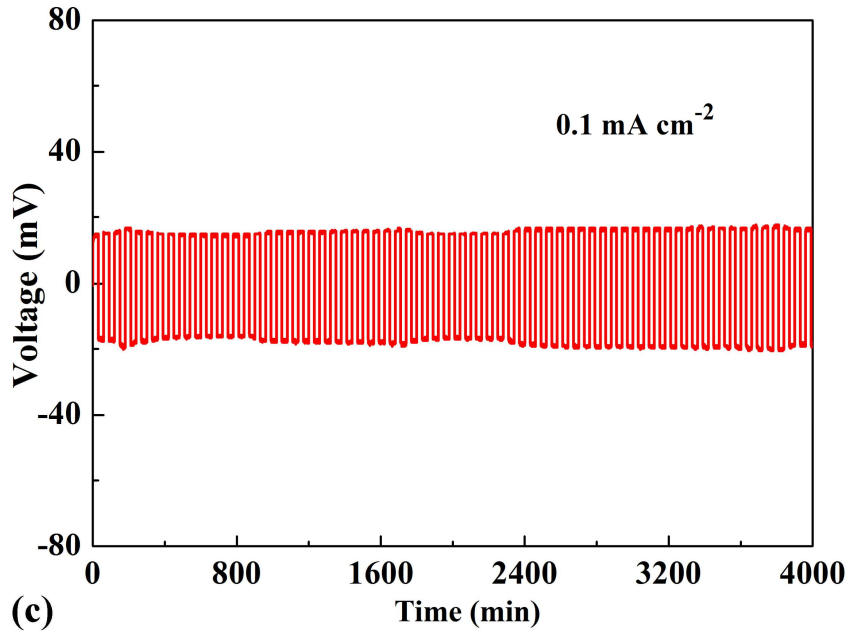
(b)
0.1 mA cm-2
Voltage (mV)
Time (min)

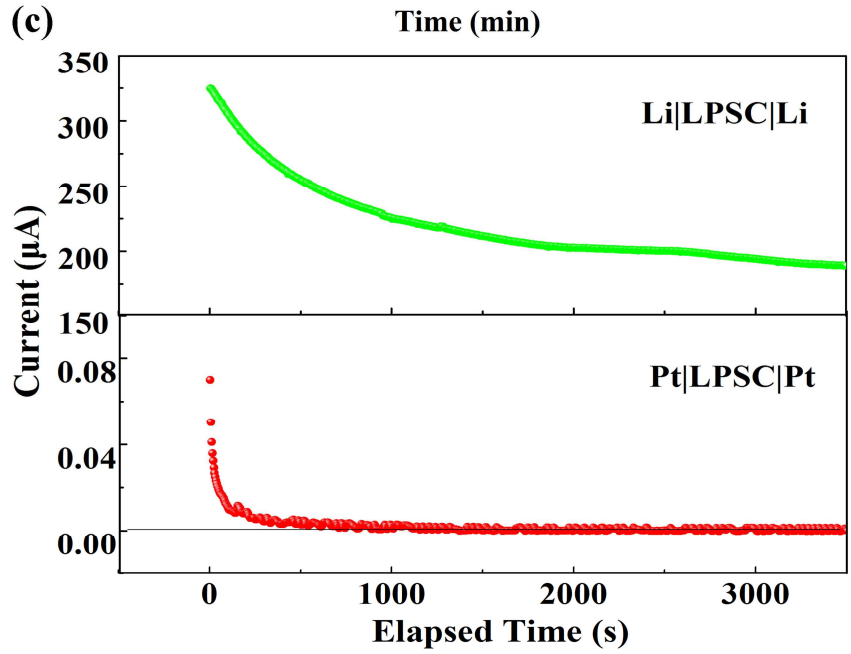
(c)
Li|LPSC|Li
Pt|LPSC|Pt
Current (μA)
Elapsed Time (s)

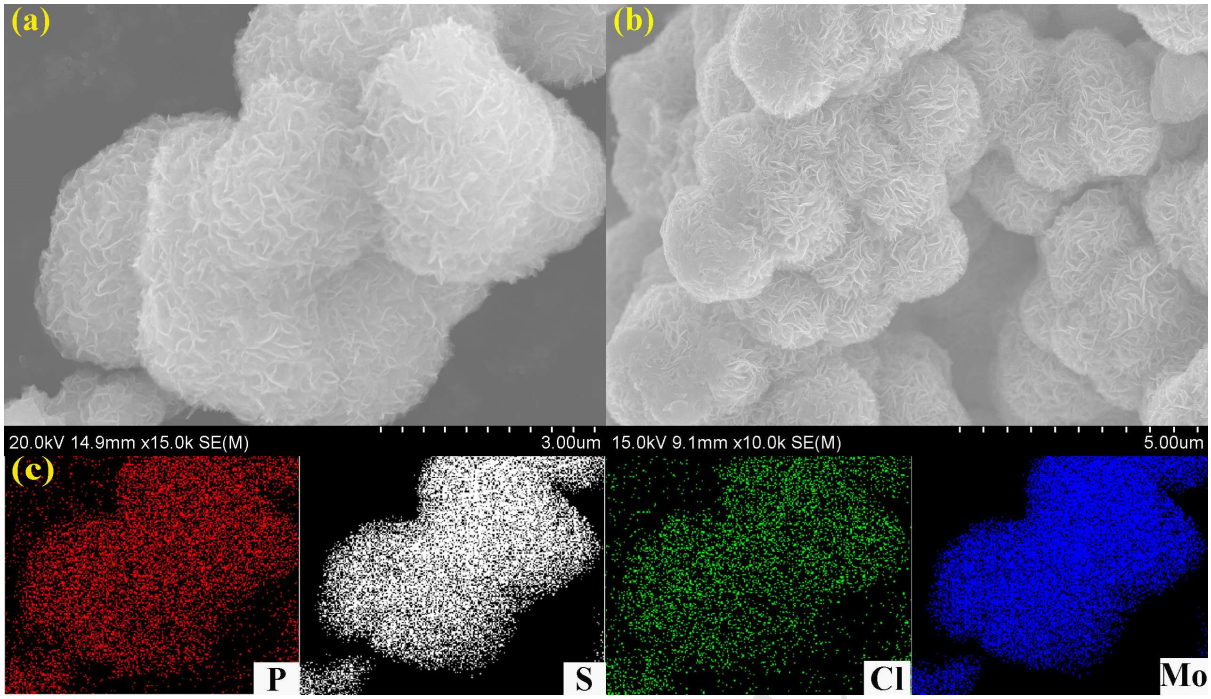

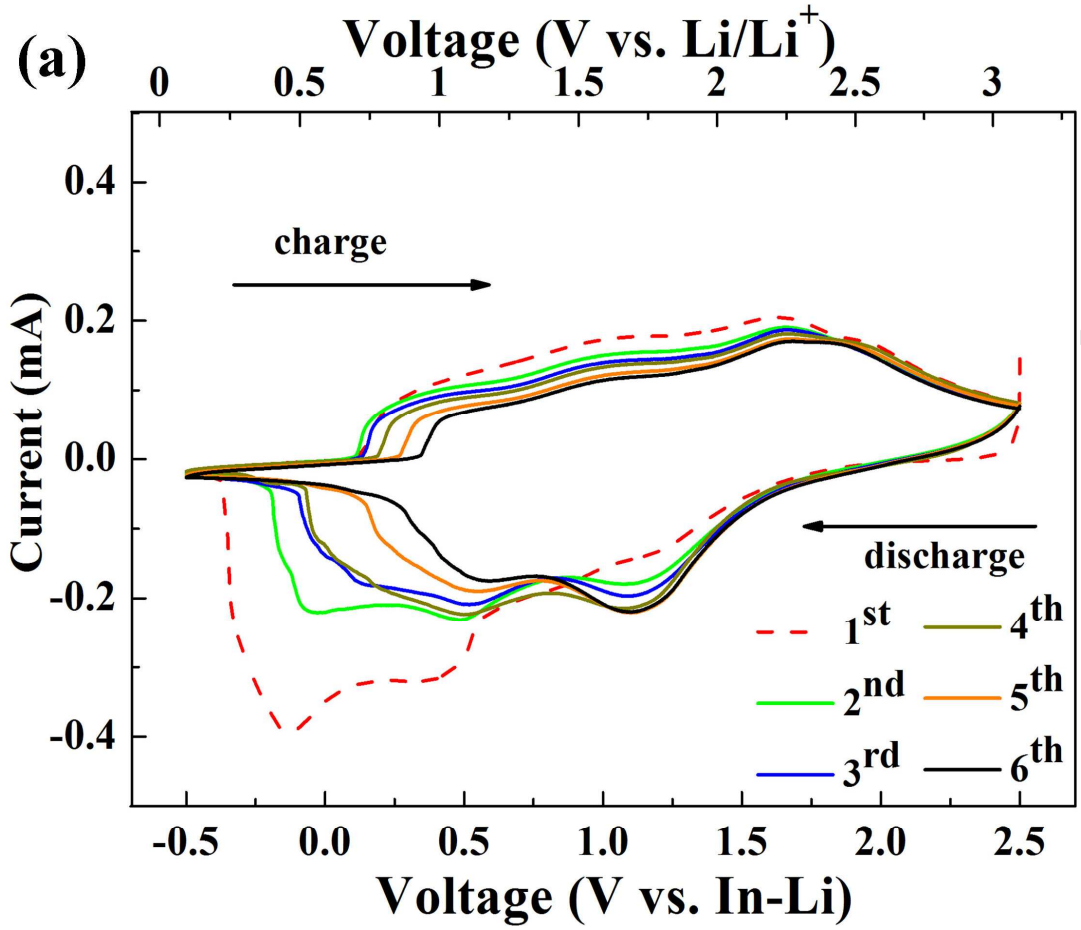
(a)
Voltage (V vs. Li/Li+)
0
0.5
1
1.5
2
2.5
3
0.4
0.2
0.0
-0.2
-0.4
Current (mA)
charge
discharge
1st
2nd
3rd
4th
5th
6th
-0.5
0.0
0.5
1.0
1.5
2.0
2.5
Voltage (V vs. In-Li)

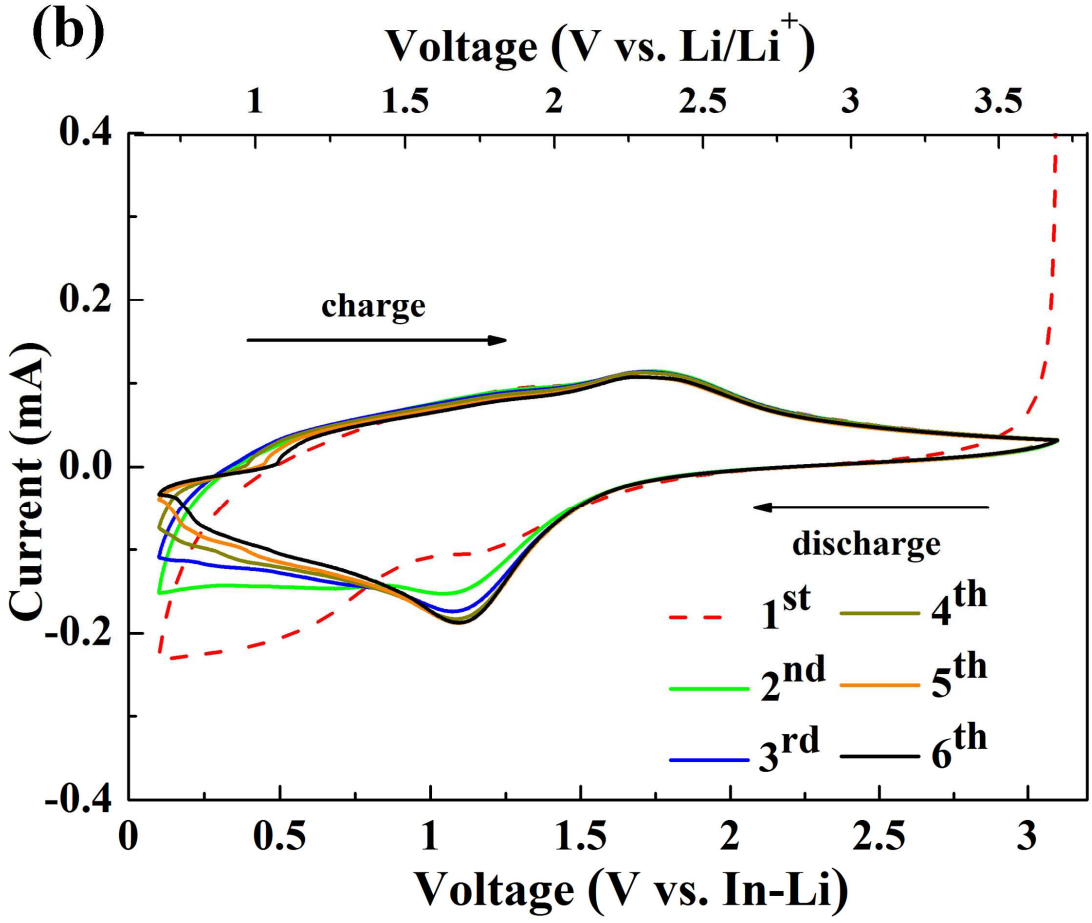
(b)
Voltage (V vs. Li/Li+)
1
1.5
2
2.5
3
3.5
0.4
0.2
0.0
-0.2
-0.4
Current (mA)
charge
discharge
1st
2nd
3rd
4th
5th
6th
0
0.5
1
1.5
2
2.5
3
Voltage (V vs. In-Li)

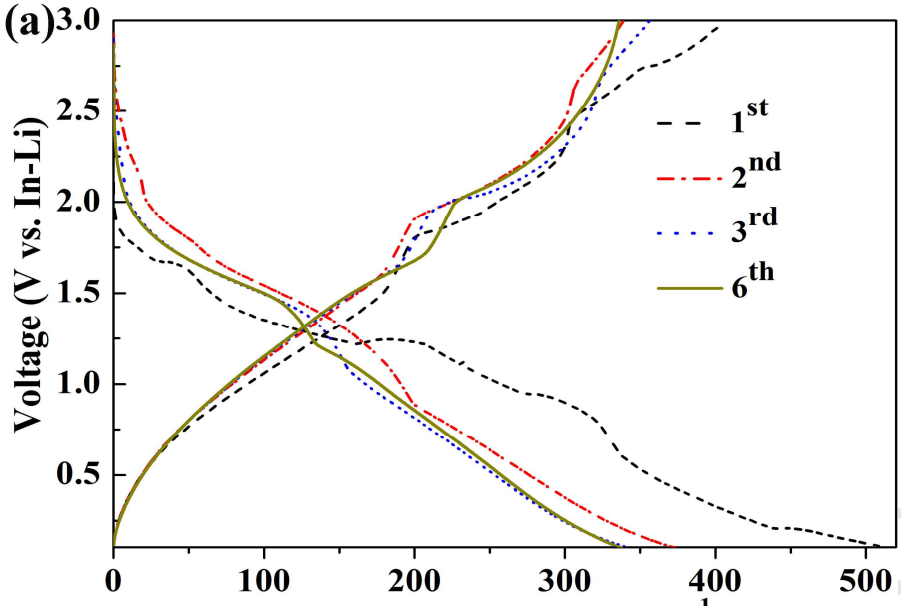
(a)
Voltage (V vs. In-Li)
Specific capacity (mAh g-1)
1st
2nd
3rd
6th

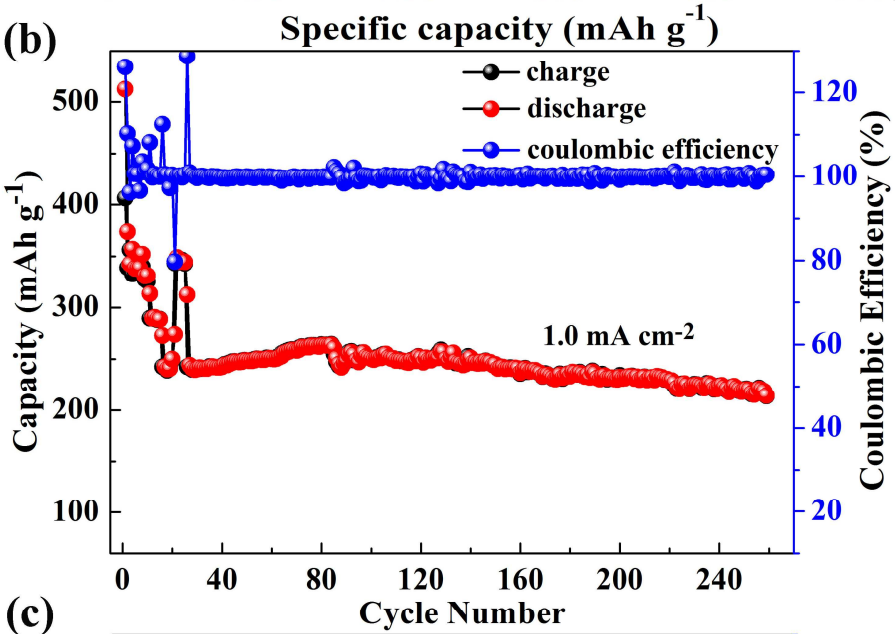
(b)
charge
discharge
coulombic efficiency
1.0 mA cm-2
Capacity (mAh g-1)
Coulombic Efficiency (%)
Cycle Number

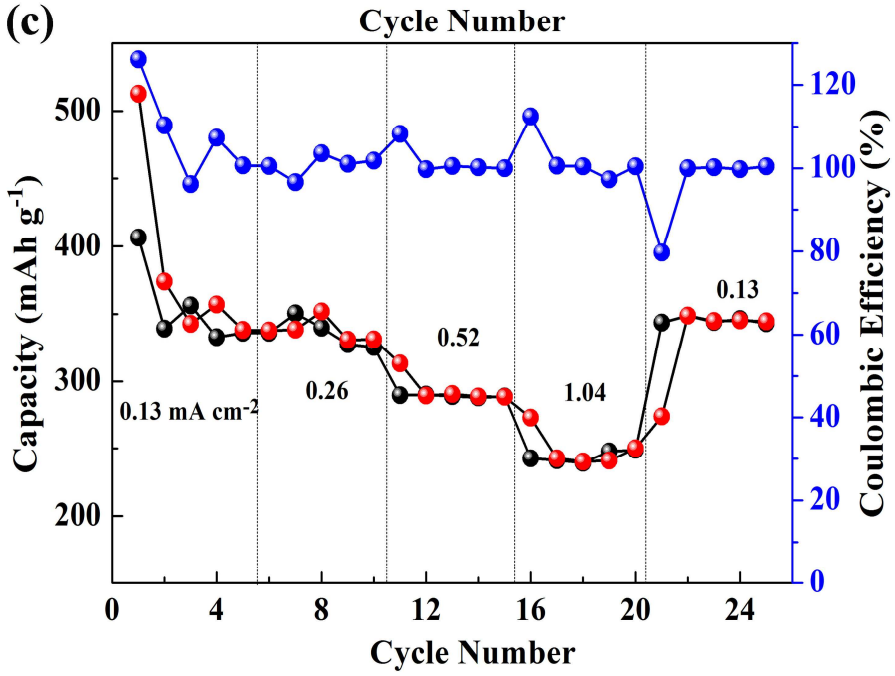
(c)
0.13 mA cm-2
0.26
0.52
1.04
0.13
Capacity (mAh g-1)
Coulombic Efficiency (%)
Cycle Number

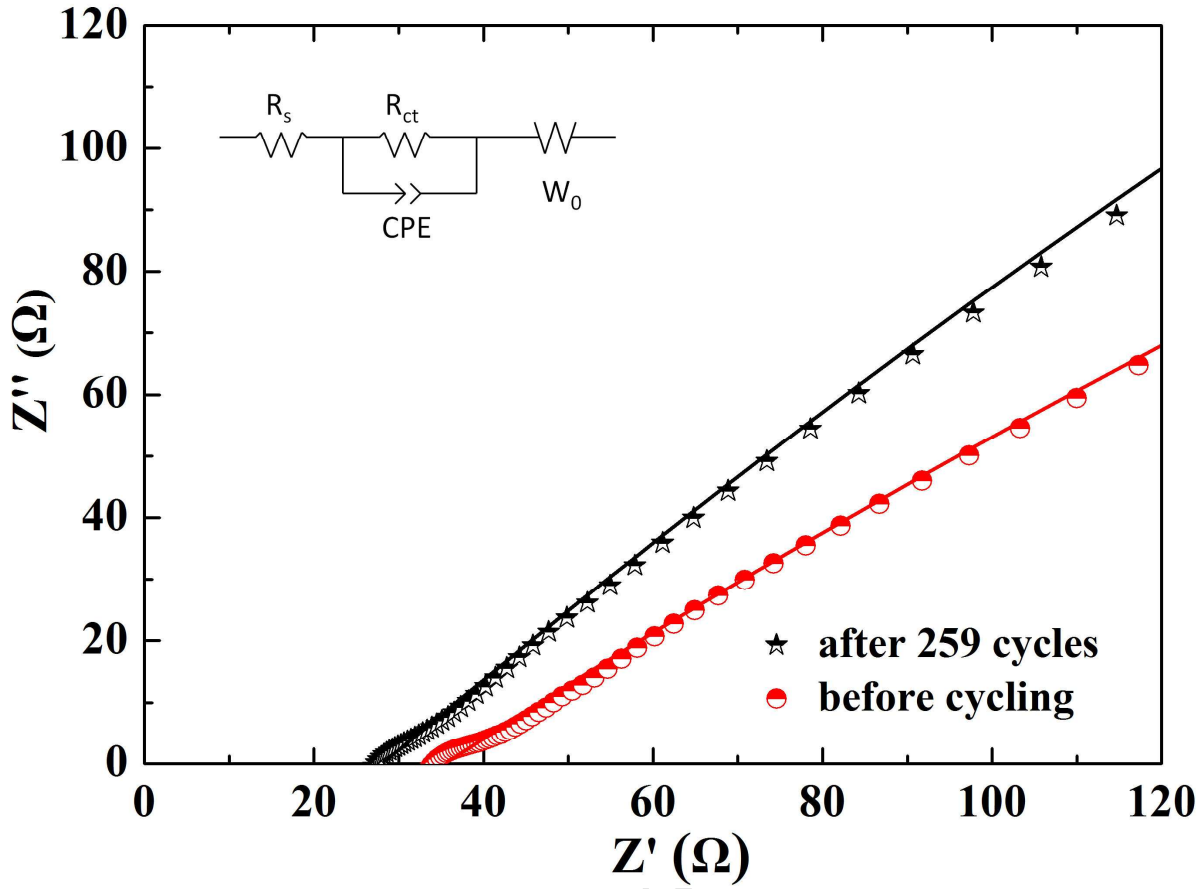

- Li_6PS_5X is compared for various X elements and synthesis methods.
- The strategy toward excess of Li_2S is illuminated.
- The morphology of Li_6PS_5X is controlled by various synthesis techniques.
- Li_6PS_5Cl can sustain air exposure for a certain time.
- Li_6PS_5Cl-based all-solid-state batteries show good electrochemical performance.